Available online at www.sciencedirect.com

ScienceDirect

IFAC Papers Online CONFERENCE PAPER ARCHIVE

IFAC PapersOnLine 59-20 (2025) 470–475

Tail-Propeller Assisted UAV Perching Control System Design & Verification ⋆

Roberto Farinango Limaico * **Jongrae Kim** * **Bilal Kaddouh** *

* *School of Mechanical Engineering, University of Leeds, Leeds LS2 9JT, UK (e-mail: [mnrcfl, menjkim, b.kaddouh]@leeds.ac.uk).*

Abstract: Fixed-Wing Unmanned Aerial Vehicles (FW-UAVs), requiring a runway for landing, provide better performance than multi-rotor UAVs and Vertical Take-Off and Landing (VTOL)-FW-UAVs in endurance, range and energy efficiency. To benefit from the efficiency of a FW-UAV and the convenience of a VTOL-UAV, this work proposes a runway-less landing approach by executing a flare and perching manoeuvre. The landing trajectory is optimised by solving the optimal control problem for the perching manoeuvre. Open-loop experiments revealed significant deviations from the target flight path and a high pitch angle at touchdown as expected. This paper introduces a Time-Varying Linear Quadratic Regulator (TVLQR) controller designed to correct deviations of the flight path from the optimal trajectory. The TVLQR reduces the mean absolute error of the deviations and increases the success rate to 60%. It shows, however, the final pitch angle remains as high as 57°, leading to tail collisions. Introducing a tail rotor with a 45° activation threshold further improves the performance, reducing the final pitch angle to 25° and increasing the success rate to 77%. The performance of the system is evaluated and presented including it's ability to maintain pitch stability under wind disturbances. Data from 120 indoor flight tests confirm the effectiveness of combining feedback control with auxiliary thrust, demonstrating robustness to aerodynamic disturbances.

Keywords: Perching Landing, Optimal Flight Path, Linear Quadratic Regulator, Tail Rotor

1. INTRODUCTION

Unmanned Aerial Vehicles (UAVs) have demonstrated remarkable versatility in a wide range of applications, from surveillance and delivery services to environmental monitoring and disaster response. While multi-rotor UAVs are valued for their hovering, manoeuvrability, and vertical take-off and landing capabilities, fixed-wing UAVs offer superior performance, including higher endurance, range, energy efficiency, and increased payload capacity; making them ideal for extended missions such as large-scale environmental monitoring and long-range parcel delivery. Despite these advantages, the usage of fixed-wing has been restricted in complex or urban environments due to their limitations in deployment and recovery, limiting their adoption compared to multi-rotors; for instance, in 2017, only 3% of mapping activities used fixed-wing platforms (Drone-Deploy, 2017). The deployment and recovery of fixed-wing UAVs face significant challenges, particularly in complex or urban environments where runway availability is limited.

To address runway limitations, hybrid UAV platforms combining vertical take-off and landing features of multi-rotors and fixed-wing capabilities have been developed. Different concepts such as quad-planes, tail sitters, and tilting motors improve flexibility but often introduce penalties like added weight, drag, and mechanical complexity, reducing in general fixed-wing performance advantages (Kim and Park, 2022; Gryte et al., 2021; Bornebusch and Johansen, 2021; Moore et al., 2014).

Parachute systems have shown scalability, but have faced problems with accuracy and precision in windy conditions, which is unacceptable for recovery with limited landing space (Wyllie, 2001). Net recovery systems have shown higher landing accuracy, however, their high impact forces in collision make them unsuitable for delicate aircraft and hardly scalable in heavy aircraft (Fahlstrom and Gleason, 2012). A similar problem is found with the arresting line systems, as their high impact loads and lack of deceleration control at capture required the implementation of additional reinforcement or specialized airframes able to handle the large loads (Skitmore, 2020). The use of the rail concept was proposed as a solution to decelerate the aircraft in a controlled manner (Schweighart et al., 2020; Müller et al., 2022), but its use in heavy aircraft may be limited by the required horizontal length of the rail, which may not be available in some complex environments.

An ideal runway-less landing system would enable precise landings, efficiently dissipate kinetic energy, and avoid complex airframe modifications, thus maintaining the inherent benefits of fixed-wing UAVs while enhancing their operational flexibility in challenging environments. Among runway-less landing methods, biologically inspired perching stands out by transforming kinetic energy into potential energy, rather than dissipating it mechanically (Crowther, 2000; Venkateswara Rao et al., 2015; AliKhan et al., 2013).

⋆ This research is funded by the Engineering and Physical Science Research Council (EPSRC) [EP/W524372/1] and [EP/V026801/1].

10.1016/j.ifacol.2025.11.195

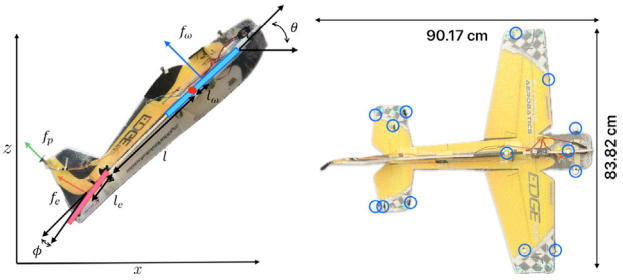

Fig. 1. The glider and the markers for measuring the position and the attitude using the cameras

The perching technique offers unique advantages, including the ability to relaunch using stored potential energy, making it ideal for surveillance missions on natural or urban structures (Crowther, 2000; Wickenheiser and Garcia, 2008). Additionally, it eliminates the need for traditional infrastructure, e.g., runways, hooks or nets, and can reduce the weight and drag of the aircraft by allowing the removal of conventional landing gear (Greatwood et al., 2017). These benefits translate into greater payload capacity or extended endurance.

Early research, such as Crowther and Prassas (1999), demonstrated the feasibility of post-stall landings through numerical simulations, highlighting that headwinds can ease the flare manoeuvre and that aircraft with low wing loading, less than 100 N/m^2, are ideally suited for post-stall landing. Later studies reinforced the complexity of achieving optimal perching trajectories, emphasizing the high precision required in guidance and control (Crowther, 2000). Perched landing recovery involves executing an extended flare manoeuvre to achieve near-zero forward speed. By pitching up, the fixed-wing aircraft increases its angle of attack, converting kinetic energy into potential energy as it ascends. At the peak, the aircraft stalls and is captured. The goal is to achieve minimal vertical and horizontal velocities during capture, however, the main challenge is to maintain control during deceleration.

Various control strategies have been explored to address this issue, including a singularity-free online neural network-based sliding mode controller (Song et al., 2023), nonlinear model predictive control and Linear Quadratic Regulator (LQR)-Trees (Moore et al., 2014). In their comparison of the latter two methods via indoor experiments, Moore et al. (2014) found that LQR-Trees are better suited for real-time applications due to their lower computational demands and improved handling of model uncertainties and have demonstrated the LQR-Trees achieving a 95% success rate over 147 flights. To counteract reduced control authority during low-speed phases, Song et al. (2023) recommended exploring new aircraft configurations with an auxiliary control mechanism to physically improve control authority. In this paper, we introduce a novel runway-less method that combines perching manoeuvres with a tail-mounted propeller for improved control authority to compensate for trajectory errors, enhancing landing precision and safety.

The remainder of this paper is organized as follows: firstly, we present the glider's dynamic model, the optimal trajectory design, and the LQR controller formulation; secondly, the details of the experimental setup and the verification results are presented; and finally, conclusions and future works are presented.

Table 1. Glider Parameters

Quantity	Symbol	Units	Value
Glider mass	m	kg	0.096
gravitational acceleration	g	m/s^2	9.81
air density	ρ	kg/m^3	1.125
Wing area	Sw	m^2	0.1122
Elevator area	Se	m^2	0.0258
Glider inertia	Iyy	kg·m^2	0.0015
Location of tail leading-edge	l	m	0.222
Wing moment arm	lw	m	0.0464
Elevator moment arm	le	m	0.05

2. CONTROL DESIGN

In this section, the dynamics of the glider is summarised. The offline optimal flight path is designed using non-linear predictive control and the time-varying LQR (TVLQR) is designed as a feedback controller.

2.1 Flat Plate Glider Dynamics

Following the approach presented in Moore et al. (2014), Cory and Tedrake (2008), and Roberts et al. (2009), the glider is modelled as a single rigid body subject to gravitational and aerodynamic forces. Roll and yaw angles maintain constant reducing the aircraft dynamics to a 7-state system represented by

$$d\mathbf{x}/dt = \mathbf{f}(\mathbf{x}, u) \tag{1}$$

where $d\mathbf{x}/dt$ is the time derivative of $\mathbf{x}$, t is the time in seconds, $\mathbf{f}(\mathbf{x}, u)$ includes the kinematics and the rigid-body dynamics with the control actions, aerodynamic force and the gravitational force, the state vector, $\mathbf{x}$, is defined by

$$\mathbf{x} = \begin{bmatrix} x & z & \theta & \phi & \dot{x} & \dot{z} & \dot{\theta} \end{bmatrix}^T \tag{2}$$

$\dot{(\cdot)} = d()/dt$, t is the time in seconds, $[\cdot]^T$ is the transpose, x and z represent the position coordinates in the horizontal forward positive and the vertical upwards positive in meters, respectively, and θ is the pitch angle in radians. u represents the control input, which is given by the rate change of the elevator, $\dot{\phi}$, where ϕ is the elevator deflection angle in radians.

The translational motion dynamics is given by

$$m\ddot{x} = -f_w \sin\theta - f_e \sin(\theta + \phi) \tag{3}$$

$$m\ddot{z} = f_w \cos\theta + f_e \cos(\theta + \phi) - mg \tag{4}$$

where m is the mass of the glider, g is the gravitational acceleration, 9.81 m/s, f_w and f_e are the normal components of the aerodynamic forces on the wing and the elevator, respectively, given by

$$f_w = \rho \dot{x}_w^2 S_w \sin(\alpha_w), \;\; f_e = \rho \dot{x}_e^2 S_e \sin(\alpha_e) \tag{5}$$

ρ is the air density, S_w is the wing surface area, α_w and α_e are the wing and the elevator's angle of attack, respectively, given by

$$\alpha_w = \theta - \tan^{-1}(\dot{z}_w/\dot{x}_w) \tag{6a}$$

$$\alpha_e = \theta + \phi - \tan^{-1}(\dot{z}_e/\dot{x}_e) \tag{6b}$$

The coordinates of the geometric centroids of the wing and elevator are (x_w, z_w), (x_e, z_e), respectively.

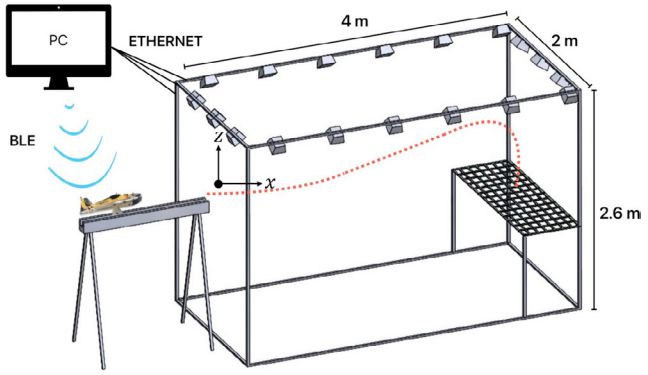

Fig. 2. Ethernet connection between the PC and the cameras; Bluetooth Low Energy (BLE) connection between the computer and the glider onboard computer

The rotational dynamics is given by

$$I\ddot{\theta} = -f_w l_w - f_e(l_w \cos\theta + l_e) \tag{7}$$

where I is the moment of inertia of the glider about the centre of mass, l_w is the moment arm of the wing and l_e is the moment arm of the elevator. The full details of $\mathbf{f}(\mathbf{x}, u)$ and its derivations can be found in Moore et al. (2014); Cory (2010); Roberts et al. (2009). The glider configurations and the markers to measure the position and attitude of the glider are shown in Figure 1, and the physical parameters are summarised in Table 1.

2.2 Optimal Trajectory Design

The first step in the perching manoeuvre involves computing a nominal trajectory for the system using standard trajectory optimization techniques. Despite the nonlinear and under-actuated nature of the glider dynamics, these techniques provide effective solutions for computing a locally optimal trajectory.

We employ the Hermite-Simpson Direct Collocation method, implemented using the Trajectory Optimization Library from Kelly (2023). This method is preferred over shooting-based approaches as it treats both the system states and control inputs as optimization variables, allowing for explicit constraints on both states and inputs (Moore et al., 2014).

The optimization problem is formulated as follows:

$$J_{\text{OT}} = \sum_{n=0}^{N-1} Ru_n^2 + \mathbf{x}_n^T Q \mathbf{x}_n \tag{8}$$

subject to the system dynamics: $\mathbf{x}_{n+1} = \mathbf{x}_n + h\mathbf{f}(\mathbf{x}_n, u_n)$, where Q is the state cost matrix, R is the control cost, h is the time step size, which is equal to 50 ms, u_n is the control input $u(t)$ at n-th time step and $\mathbf{x}_n$ is the state $\mathbf{x}(t)$ at n-th time step, i.e., $t = nh$.

We choose $Q = 10I_7$, where I_7 is the 7×7 identity matrix, and $R = 100$, taken from Moore et al. (2014). The objective function is designed to find the optimal trajectory with the minimum control to reach a target from an initial point.

The initial states are given by: $x(0) = 0.5$ m, $z(0) = 1.5$ m, $\theta(0) = 0.0$, $\phi(0) = 0.0$, $\dot{x}(0) = 7.0$ m/s, $\dot{z}(0) = 0.0$ and $\dot{\phi}(0) = 0.0$. The final state is constrained by $x(t_f) = 3.6$ m, $z(t_f) = 1.0$ m, $0.0 \leq \theta(t_f) \leq 45°$, $0.0 \leq \dot{x}(t_f) \leq 2$ m/s, $-2.0 \leq \dot{z}(t_f) \leq 0.0$ m/s and the elevator angle $\phi(t_f)$ and its rate $\dot{\phi}(t_f)$ are constrained on the range of $[-60°, 22.5°]$ and $\pm 744.8°$/s, which corresponds to the servo maximum velocity, respectively, where the final time, t_f, is equal to 1 s.

By solving this optimization problem, we obtain the optimal trajectory, $\mathbf{x}^*(nh)$, and the optimal control input $u^*(nh)$ for $n = 0, 1, 2, \ldots, N-1$, with $N = 21$, that serves as the basis for the LQR-Trees. The results are presented in Figure 3, showing the orange curve as an optimal perching trajectory under these constraints.

2.3 LQR Controller

We linearise the non-linear dynamics around the optimal perching trajectory, obtain a time-varying linear model and design a TVLQR controller.

Linearise (1) along the optimal trajectory as follows:

$$\dot{\bar{\mathbf{x}}}(t) = A(t)\bar{\mathbf{x}}(t) + B(t)\bar{u}(t) \tag{9}$$

where $\bar{\mathbf{x}}(t)$ is equal to $\mathbf{x}(t) - \mathbf{x}^*(t)$, represents deviations from the nominal trajectory, $\mathbf{x}^*(t)$ is the interpolation using $\mathbf{x}^*(nh)$, $\bar{u}(t)$ is equal to $\dot{\phi} - u^*(t)$, $u^*(t)$ is the interpolation using $u^*(nh)$, and $A(t)$ and $B(t)$ are the Jacobian matrices of $\mathbf{f}(\mathbf{x}, u)$ along $\mathbf{x}^*(t)$ and $u^*(t)$.

The TVLQR control law is obtained by minimizing the following quadratic cost function:

$$J_{\text{LQR}} = \bar{\mathbf{x}}_f^T Q_f \bar{\mathbf{x}}_f + \int_0^{t_f} \bar{\mathbf{x}}^T Q_{\text{LQR}} \bar{\mathbf{x}} + \bar{u}^T R_{\text{LQR}} \bar{u}\, dt \tag{10}$$

where $\bar{\mathbf{x}}_f = \bar{\mathbf{x}}(t_f)$

The state cost matrix for the LQR design $Q_{\text{LQR}} = \text{diag}[10I_3, I_4]$, and the final state cost matrix $Q_f = \text{diag}[400I_2, 1/9I_2, I_2, 1/9]$ were adopted from Moore et al. (2014), where they were originally selected to encourage the system to remain close to the nominal trajectory—where linearisation is valid—and to ensure well-conditioned Riccati solutions over a reasonable range of initial conditions.However, through our experiments, we found that increasing the control cost matrix, R_{LQR}, to 30, which penalises control effort more, resulted in improved performance, by reducing excessive actuator usage.

Solving the following differential Riccati equation (DRE) at every control step from $t_f = 1$ to the current time

$$-\dot{S}(t) = Q - S(t)BK + S(t)A + A^T S(t) \tag{11}$$

with $S(t_f = 1) = Q_f$ yields the optimal TVLQR control law as follows: $\bar{u}(t) = -R^{-1}B^T S(t)\bar{\mathbf{x}}(t) = -K\bar{\mathbf{x}}(t)$. The steps and control strategy outlined here are based on Moore et al. (2014).

3. PERCHING PERFORMANCE VERIFICATIONS

In this section, the experiment setup for verifying the perching performance is introduced and the four cases of verification experiments are performed and discussed.

3.1 Experiment Setup

The indoor flight experiment area is equipped with a vision capture system consisting of eighteen Prime 41 cameras to

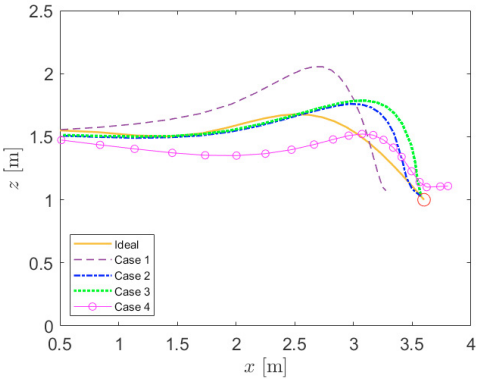

Fig. 3. Example flight path, x-z, for each case.

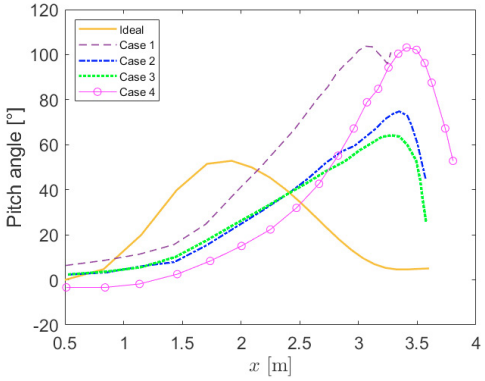

Fig. 4. Example pitch angle, θ, along x.

cover a capture volume of 2 m×4 m×2.6 m. These cameras track the position, velocity, and orientation of the aircraft by detecting a set of reflective markers affixed to the glider as shown in Figures 1 and 2. A total of 14 reflective markers are placed on the fuselage and elevator—eight on the fuselage and six on the elevator. The camera measurements are transmitted to the computer at 120 Hz.

The glider used is the EDGE 540 Mini model from Twisted Hobbies, modified to operate without onboard propulsion except for an additional small propeller mounted at the end of the tail. This propeller serves as an auxiliary control mechanism to improve manoeuvrability during the perching approach, along with the elevator, which is actuated by a Hitec HS-45HB servo. The glider's total weight is 85 g, with a centre of gravity located 19.5 cm from the nose. The aerodynamic characteristics are modelled with the centre of gravity positioned 2.392 cm behind the aerodynamic centre of the wing and 24.7 cm from the aerodynamic centre of the tail.

The data processing and communication system employs a dual-computer setup. The main computer, connected to the router, exclusively runs Matlab processing the measurements and generating control commands. The control inputs are sent to the glider using a Bluetooth Low-Energy (BLE) connection. The OptiTrack software runs on a secondary computer, which streams the captured camera data over a local network via a TP-Link Archer C3150 router.

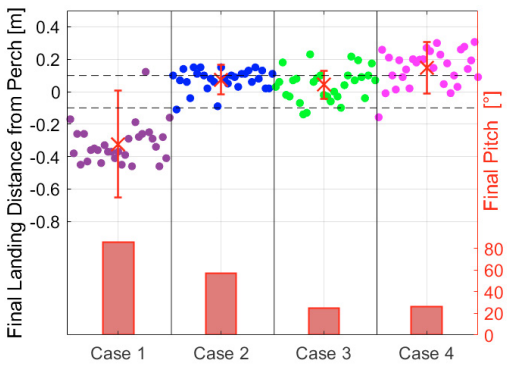

Fig. 5. The average landing points indicated by the red × and the error bars representing the mean-absolute-error for each case. The bars below showing the average pitch angle at the landing.

The aircraft enters the capture volume with an initial speed of 7 m/s using a controlled launching mechanism. On board Arduino Nano 3.3 BLE Rev2 microcontroller, powered by a 2S LiPo battery through a Battery Eliminator Circuit (BEC), of the glider processes the commands and executes the tail movement and propeller activation in the frequency of 21 commands/s.

The glider is launched at a distance of 3.1 m and 0.5 m altitude difference from the perch with an initial speed of 7 m/s. It then executes a high angle of attack manoeuvre to decelerate to zero velocity in 1 s. we defined as successful perching manoeuvre when glider lands within ±10 cm of the target point.

3.2 Results

A series of 30 test trials were conducted for each experimental scenario shown in Table 2. Case 1 is with the open-loop control and the other three are with the closed-loop control. Case 2 is without the tail rotor activated and Cases 3 and 4 are with the tail rotor activated. Finally, Case 4 is the closed-loop control with the tail rotor activated and wind gust applied. *Case 1:* The initial experiment assessed the aircraft's performance without position feedback control, i.e., open-loop. The results showed that, in this configuration, the glider landed significantly far from the target, with a final x coordinate of 3.24 m, as shown in Figure 3. Additionally, the high final pitch angle, 86°, shown in Figure 4, and the final velocity, 0.92 m/s, indicated that the glider was unable to recover effectively, often stalling before reaching the landing area. This leads to poor accuracy and a 0% success rate in landing within the designated target range.

Table 2. Experiment Cases & Success Rates

Case	Controller	Propeller	Wind	Success
1	Open-Loop	No	No	0%
2	TVLQR	No	No	60%
3	TVLQR	Yes	No	77%
4	TVLQR	Yes	Yes	33%

Case 2: Implementing the closed-loop controller significantly improved the landing accuracy and stability. The final x coordinate improved to 3.67 m, only 7 cm beyond

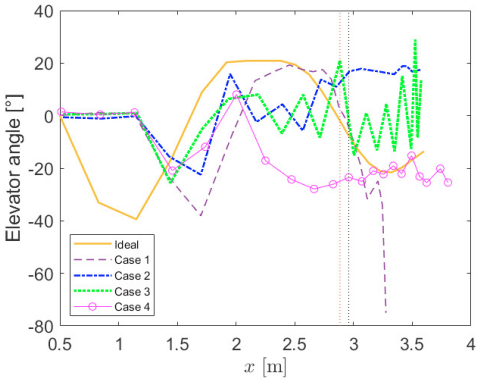

Fig. 6. Elevator angle, ϕ, along x. Two vertical dotted lines indicate the tail propeller activated.

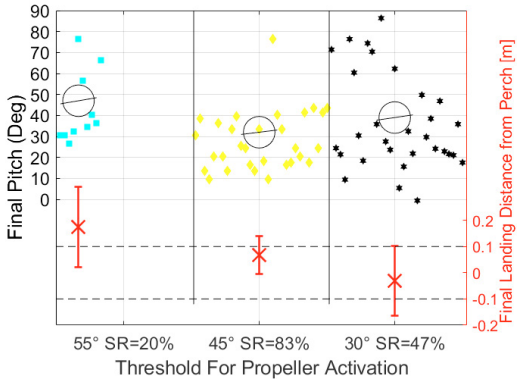

Fig. 7. Final pitch angle for each threshold, showing the average pitch angle as the large circle. The crosses with the error bars represent the average landing point and the MAE. The Success Rate (SR) is shown as a percentage on the horizontal axis.

the target as shown in Figure 3. The mean absolute error (MAE) reduced from 36.5 cm for Case 1 to 9 cm, as shown in Figure 5, and the success rate increased from 0% to 60%, as indicated in Table 2.

A clear difference from Case 1 is evident in the x-z trajectories, shown in Figure 3. The closed-loop trajectory remains close to the ideal precomputed trajectory until it reaches the 2.5 meters, whereas the open-loop trajectory deviates significantly almost from the beginning.

Comparing the elevator angle state against the ideal case on Figure 6, the open-loop response exhibits a rightward shift, indicating a delay between the control command and the actual execution. In contrast, the TVLQR controller mitigates this delay and reduces the initial pitch-up command from -38° to -22°, helping to keep the glider on the ideal trajectory while avoiding excessive pitch angles that could lead to loss of control. The effect of the TVLQR controller on pitch dynamics is evident in Figure 4, which shows the pitch angle variation with respect to x-coordinate. Without control, the pitch angle increases to over 90°, causing an early stall or even a rollover of the glider. In contrast, with closed-loop control, Case 2, the pitch angle is effectively managed, resulting in a final pitch angle of 57°, demonstrating improved stability. Additionally, the final velocity increased to 2.37 m/s due to the control effort required for trajectory correction.

Despite the improvements achieved with closed-loop in Case 2 the final pitch angle remained high, 57°, leading to an unfavourable touchdown attitude. Since the glider is captured by an horizontal net, excessive pitch angles cause the tail to impact first, concentrating the landing force on the tail, increasing the risk of structural damage. Additionally, while the TVLQR controller effectively reduced pitch excursions, it relied solely on aerodynamic control surfaces, which have limited authority at low speeds, particularly in the final stages of the landing trajectory.

To ensure a safer landing and better distribute impact force along the belly of the glider, a tail rotor was introduced to actively assist in pitch corrections. By reducing the pitch angle before touchdown, the glider can achieve a more horizontal alignment with the net.

Case 3: A small propeller was introduced to assist in pitch recovery, activating when the glider exceeded a pre-defined pitch threshold. This threshold defines the specific pitch angle at which the propeller engages to provide corrective thrust, preventing excessive nose-up attitudes before touchdown. Proper threshold selection is critical—activating too early may cause unnecessary energy consumption and instability, while a delayed response may fail to correct the pitch in time. In this study, three threshold angles, i.e., 55°, 45°, and 30°, are tested to evaluate their effect on landing accuracy and stability. Results showed in Figure 7 indicates that the 45° threshold provides the best balance, effectively reducing pitch excursions while maintaining a high success rate.

Both the 45° and 30° thresholds resulted in an average landing point within the perch zone, as indicated by the error bars in Figure 7. However, despite the 30° threshold appearing closer to the target, it exhibited greater MAE, as shown by the error bars. Additionally, the success rate was significantly lower, 47% for the 30° threshold vs. 83% for the 45° threshold, eliminating the 30° setting as a viable option.

With the propeller activated at 45°, the final x-coordinate improves slightly to 3.64 m, and the success rate increases to 77%. The MAE decreases by 0.3 cm compared to the closed-loop configuration without the propeller. The most significant effect is on the final pitch angle, which decreases from 57° to 25°, as shown in the lower part of Figure 5, demonstrating improved alignment for landing. However, the propeller's activation also results in a slightly higher final velocity, 2.78 m/s, due to the additional thrust applied during recovery.

The vertical dotted line in Figure 6 indicates the point at which the propeller is activated. Its effect on pitch dynamics can be observed in Figure 4, where a notable reduction in pitch angle occurs from the activation point to the end of the trajectory.

Case 4: The final test introduces wind disturbance to evaluate the robustness of the system under external perturbations. The final x-coordinate deviates by 14 cm compared to the previous test but still performs significantly better than the open-loop case. The MAE increases from 9 cm (closed-loop) to 16 cm, as shown in Figure 5, and the

success rate drops to 33%, showing that wind disturbances negatively impacts landing accuracy.

Despite the increased error, the propeller-assisted configuration still demonstrates advantages. Although the average landing point is 4 cm beyond the perch zone, and the success rate is lower, the propeller effectively assisted in pitch recovery, maintaining an average pitch angle of 26°, comparable to the 25° observed in Case 3.

Figure 4 illustrates how, despite increased pitch oscillations due to wind, the propeller effectively counteracts excessive pitch excursions, helping the glider return to a stable descent. Additionally, the final velocity decreases slightly to 2.21 m/s, suggesting that the disturbances caused a minor reduction in energy dissipation during landing.

4. CONCLUSIONS & FUTURE WORKS

Open-loop tests result in significant deviations from the target due to the lack of correction mechanisms, often leading to stalling and unsuccessful landings. The TVLQR closed-loop configuration significantly improves trajectory tracking, reduces the MAE, and increases the success rate. However, despite this improvement, the controller tends to bring the aircraft to touchdown at a high pitch angle, causing it to land on its tail rather than its belly, which compromises the structural integrity of the glider. The introduction of a small propeller for pitch correction further enhances the system's performance by assisting in attitude recovery and stabilizing the descent phase. The results highlight the importance of selecting an optimal activation threshold, as inappropriate values could lead to reduced accuracy or lower success rates. Additionally, while wind disturbances negatively affects landing precision, the closed-loop system with propeller assistance demonstrates increased robustness against external perturbations.

Future works will focus on integrating a moving platform to compensate for the remaining deviations observed in landing accuracy, allowing the minimisation of the landing platform and testing in outdoor environments.

ACKNOWLEDGEMENTS

The authors would like to express our appreciation to the EPSRC for providing the grants [EP/W524372/1] and [EP/V026801/1] for the research.

REFERENCES

AliKhan, M., Peyada, N.K., and Go, T.H. (2013). Flight dynamics and optimization of three-dimensional perching maneuver. *Journal of Guidance, Control, and Dynamics*, 36(6), 1791–1796. doi:10.2514/1.58894.

Bornebusch, M.F. and Johansen, T.A. (2021). Autonomous recovery of a fixed-wing uav using a line suspended between two multirotor uavs. *IEEE Trans. on Aerospace and Electronic Systems*, 57(1), 90–104.

Cory, R. and Tedrake, R. (2008). Experiments in fixed-wing UAV perching. In *AIAA Guidance, Navigation and Control Conference and Exhibit, 18-21 August 2008, Honolulu, HA, USA*, 7256. doi:10.2514/6.2008-7256.

Cory, R.E. (2010). *Supermaneuverable perching*. Ph.D. thesis, Massachusetts Institute of Technology.

Crowther, W. (2000). Perched landing and takeoff for fixed wing UAVs. In *Symposium on Unmanned Vehicles for Aerial, Ground and Naval Military Operations, Conference Location: Ankara, Turkey*.

Crowther, W. and Prassas, K. (1999). Post-stall landing for field retrieval of unmanned air vehicles. In *14th Bristol International Unmanned Air Vehicle Systems Conference, Bristol, UK*.

Drone-Deploy (2017). 2017 Commercial Drone Industry Trends — DroneDeploy. URL `https://dronedeploy.com/resources/ebooks/commercial-drone-industry-trends-2017`.

Fahlstrom, P.G. and Gleason, T.J. (2012). *Launch and Recovery Tradeoffs*, chapter 19, 271–276. John Wiley & Sons, Ltd. doi:10.1002/9781118396780.ch19.

Greatwood, C., Waldock, A., and Richardson, T. (2017). Perched landing manoeuvres with a variable sweep wing uav. *Aerospace Science and Technology*, 71, 510–520.

Gryte, K., Sollie, M.L., and Johansen, T.A. (2021). Control System Architecture for Automatic Recovery of Fixed-Wing Unmanned Aerial Vehicles in a Moving Arrest System. *Journal of Intelligent and Robotic Systems: Theory and Applications*, 103(4).

Kelly, M. (2023). OptimTraj – Trajectory Optimization Library. URL `https://github.com/MatthewPeterKelly/OptimTraj`.

Kim, D. and Park, S. (2022). Vision-assisted deep stall landing for a fixed-wing uav. *Journal of Field Robotics*, 39(7), 1136–1150. doi:0.1002/rob.22100.

Moore, J., Cory, R., and Tedrake, R. (2014). Robust post-stall perching with a simple fixed-wing glider using LQR-trees. *Bioinspiration & Biomimetics*, 9(2), 025013.

Müller, J.A., Elhashash, M.Y.M.K., and Gollnick, V. (2022). Electrical launch catapult and landing decelerator for fixed-wing airborne wind energy systems. *Energies*, 15(7). doi:10.3390/en15072502.

Roberts, J.W., Cory, R., and Tedrake, R. (2009). On the controllability of fixed-wing perching. In *2009 American Control Conference*, 2018–2023. doi:10.1109/ACC.2009.5160526.

Schweighart, S., Coe, A., Ensminger, J., Giannini, F., and Pace, J. (2020). Rail recovery system for aircraft. US Patent 10,611,498.

Skitmore, A. (2020). Launch and Recovery System for Improved Fixed-Wing UAV Development in Complex Environments. In D.R. Green, B.J. Gregory, and A.R. Karachok (eds.), *Unmanned Aerial Remote Sensing*, chapter 18, 303–315. CRC Press (Taylor & Francis Group), Boca Raton, first edition edition.

Song, Y., Tang, Y., Ma, B., and Xu, B. (2023). A singularity-free online neural network-based sliding mode control of the fixed-wing unmanned aerial vehicle optimal perching maneuver. *Optimal Control Applications and Methods*, 44(3), 1425–1440.

Venkateswara Rao, D.M., Tang, H., and Go, T.H. (2015). A parametric study of fixed-wing aircraft perching maneuvers. *Aerospace Science & Technology*, 42, 459–469.

Wickenheiser, A.M. and Garcia, E. (2008). Optimization of perching maneuvers through vehicle morphing. *J. of Guidance, Control, and Dynamics*, 31(4), 815–823.

Wyllie, T. (2001). Parachute recovery for UAV systems. *Aircraft Engineering & Aerospace Technology*, 73(6), 542–551.